Journal of Global Positioning Systems (2026)
Vol. 22, Issue 2:206-222
DOI:10.5081/jgps22.2.206

Graph Convolutional Neural Networks for GNSS Multipath Mitigation in Urban Canyons via Observation and Coordinate Domains

Chenkang Cui[1], Yan Xia[1,*], Bin Wang[1]

1 School of Geomatics Science and Technology, Nanjing Tech University, Nanjing, China 211816

* Correspondence: yanx@njtech.edu.cn

Abstract: Global Navigation Satellite System (GNSS) observations from simultaneously visible satellites in urban canyons are affected by a shared local environment and exhibit structured inter satellite relationships. This study adopts a Graph Convolutional Neural Network (GCNN) to model double differenced (DD) multipath labels and evaluates two correction paths in the observation and coordinate domains. A Global Positioning System (GPS)/BeiDou Navigation Satellite System (BDS) short-baseline pseudorange DD model is used to construct the labels. The GCNN employs a hybrid adjacency rule based on constellation membership, pseudorange-residual similarity, and elevation-angle similarity. By fusing features such as pseudorange residuals, carrier-to-noise-density ratio (C/N0), line-of-sight unit vectors and elevation angles, the model predicts multipath corrections for multiple satellites within the same epoch. The experiment uses the vehicle-borne Kowloon Tong (KLT) dataset collected by the Li-Ta Hsu group in the Kowloon Tong urban canyon. In the observation domain, the GCNN achieves a multipath prediction root mean square error (RMSE) of 3.15 m, compared with 4.85 m for the Convolutional Neural Network (CNN). After applying the GCNN predictions to DD pseudorange correction, the 3D positioning RMSE is reduced from 11.01 m for the DD baseline to 8.76 m. In the coordinate domain, the GCNN achieves a 3D correction RMSE of 7.85 m, lower than the 8.84 m obtained by CNN. These results show that the GCNN outperforms the CNN in both tasks. In the present test, the coordinate-domain path yields the smaller final positioning error, whereas the observation-domain path retains the advantage of introducing physically interpretable corrections at the measurement level.

Keywords: Differential Global Navigation Satellite System (DGNSS); urban canyon; multipath mitigation; Graph Convolutional Neural Network

1. Introduction

In urban canyon environments, blockage and reflection introduce pronounced multipath/non-line-of-sight (NLOS) biases into Global Navigation Satellite System (GNSS) pseudorange observations, thereby weakening the continuity and reliability of positioning, navigation and timing (PNT) (Hsu 2017). Such biases are closely related to building geometry, satellite incidence direction, and the receiver's motion state. Their statistical distribution often deviates from a simple white-noise assumption, which makes conventional solutions prone to being pulled by outliers and strong multipath, resulting in scenario-dependent and unstable positioning errors. Existing studies have proposed a series of mitigation strategies, including consistency checks (Jiang et al. 2011), carrier-to-noise-density ratio (C/N0)-based weighting (Groves and Jiang 2013), sidereal filtering (Lu et al. 2023; Wang et al. 2018), and hemispherical maps (Dong et al. 2016; Lu et al.

Editor-In-Charge: Dr.Zeyu Li

2021). However, in dynamic traffic scenarios and under complex street-canyon blockage, the error patterns change rapidly and are difficult to parameterize with a unified model, so a usable but unstable behavior may still occur.

Unlike model-driven methods that rely on fixed a priori noise assumptions, data-driven multipath mitigation can learn systematic relationships between GNSS errors and observable signal and geometric characteristics, and can predict either observation-domain biases or position corrections (Mohanty and Gao 2024). In urban canyons, multipath and NLOS errors are jointly influenced by surrounding structures, satellite geometry, and signal quality. Previous learning-based studies have demonstrated the potential of using GNSS measurements and related contextual features to model these complex error patterns (Guillard et al. 2023; Li et al. 2024).

Within a single epoch, simultaneously visible satellites form an irregular set and may exhibit structured inter-satellite relationships because they are affected by the same local environment while having different viewing geometries and signal qualities. Fixed-size tensor representations require satellite indexing, padding, or truncation when the visible-satellite set changes across epochs. GNNs instead represent visible satellites as nodes and their relationships as edges, allowing variable-size inputs and neighborhood aggregation without forcing a fixed satellite count (Mohanty and Gao 2023; Zheng et al. 2024). Based on these considerations, this study adopts a Graph Convolutional Neural Network (GCNN) to model DD multipath errors and evaluates observation-domain and coordinate-domain correction paths. A Convolutional Neural Network (CNN) is used as a regular-tensor baseline.

This study has two main contributions. First, supervisory labels are constructed through a Global Positioning System (GPS)/BeiDou Navigation Satellite System (BDS) short-baseline pseudorange double-differenced (DD) model, avoiding direct dependence on unobservable true multipath while keeping the model outputs injectable into traditional solvers for closed-loop evaluation at the positioning level. Second, both coordinate-domain correction and observation-domain correction are examined. The coordinate-domain approach directly learns position corrections through a shorter end-to-end path, whereas the observation-domain approach predicts satellite-wise DD multipath terms and injects them back into Differential Global Navigation Satellite System (DGNSS) while preserving the observation equation structure.

2. Methods

To align with the result files and subsequent experiments, all coordinates in this study are expressed in the Earth-Centered, Earth-Fixed (ECEF) frame by default. The GCNN and CNN use consistent supervision labels and the same ground-truth source for the receiver in both the coordinate-domain and observation-domain tasks.

2.1 Problem definition and two correction paths

This study adopts two multipath-mitigation paths. The first path directly corrects the positioning solution in the coordinate domain. The second path predicts pseudorange multipath terms in the observation domain and injects them into DGNSS.

For unified notation, let $\Omega(t)$ be the set of visible satellites at epoch *t*. For any satellite $s \in \Omega(t)$, a feature vector $\boldsymbol{x}(t,s)$ can be constructed, typically including the line-of-sight (LOS) direction vector, elevation, C/N0, and pseudorange residuals derived from a geometric model. The learning problem can be formulated as learning mappings f_1 and f_2:

$$\begin{cases} f_1\left(\{\boldsymbol{x}(t,s)|\ s \in \Omega(t)\}\right) = \{\hat{m}(t,s)|\ s \in \Omega_{\text{tar}}(t)\} \\ f_2\left(\{\boldsymbol{x}(t,s)|\ s \in \Omega(t)\}\right) = \Delta\hat{\boldsymbol{p}}(t) \in \mathbb{R}^3 \end{cases} \quad (1)$$

where $\hat{m}(t,s)$ is the predicted multipath used to correct differential observations and improve the final positioning accuracy. $\Delta\hat{\boldsymbol{p}}$ is the coordinate-domain correction.

2.2 DGNSS pseudorange double-differenced solution and supervision label construction

2.2.1 GPS/BDS short-baseline DGNSS

This study adopts a short-baseline GPS/BDS pseudorange DGNSS model. For rover receiver r, base station b, target satellite i, and reference satellite k, the double-differenced (DD) pseudorange observation within the same constellation can be expressed as

$$\begin{aligned}\Delta\nabla P_{rb}^{ik} &= \Delta\nabla\rho_{rb}^{ik} + \Delta\nabla T_{rb}^{ik} \\ &+\Delta\nabla I_{rb}^{ik} + \Delta\nabla M_{rb}^{ik} + \Delta\nabla\varepsilon_{rb}^{ik}\end{aligned} \quad (2)$$

where $\Delta\nabla$ denotes between-receiver and between-satellite differencing, $\Delta\nabla\rho_{rb}^{ik}$ is the DD geometric range, T and I denote the tropospheric and ionospheric delays, respectively, M represents the equivalent pseudorange bias caused mainly by multipath/NLOS, and ε denotes measurement noise. For the short baseline considered in this study, receiver- and satellite-clock terms are eliminated by differencing, while most atmospheric common-mode errors are substantially reduced (Teunissen and Montenbruck 2017).

GPS and BDS DD observations are formed independently within their respective constellations. At each epoch, the satellite with the highest elevation angle is selected as the reference satellite for each constellation, and the same reference-satellite rule is maintained throughout DD observation construction, label generation, model training, and correction injection. Cross-system DD observations are not formed. Therefore, additional differential inter-system bias (DISB) parameters are not introduced (Ye et al 2020). Instead, the GPS and BDS DD equations are stacked and jointly solved using a common receiver position increment:

$$\begin{bmatrix}\boldsymbol{z}_G \\ \boldsymbol{z}_C\end{bmatrix} = \begin{bmatrix}\boldsymbol{H}_G \\ \boldsymbol{H}_C\end{bmatrix}\Delta\boldsymbol{p} + \begin{bmatrix}\boldsymbol{v}_G \\ \boldsymbol{v}_C\end{bmatrix} \quad (3)$$

where $\boldsymbol{H}_G$ and $\boldsymbol{H}_C$ are the GPS and BDS design matrices, respectively, and $\boldsymbol{v}_G$ and $\boldsymbol{v}_C$ contain the remaining DD observation errors.

For the positioning solution used in the subsequent correction experiments, GPS and BDS DD observations are jointly processed using a mixed weighting strategy based on satellite elevation angle and C/N0 (Tay and Marais 2013). The resulting weighted DGNSS solution is used as the common positioning baseline for both correction paths. In the observation-domain path, the predicted DD pseudorange multipath corrections are applied to the observations before weighted DGNSS positioning. In the coordinate-domain path, the position-correction labels are constructed relative to the same weighted DGNSS baseline, and the predicted corrections are directly applied to this baseline solution. This common baseline ensures a consistent comparison between the two correction paths.

An equal-weight DGNSS solution is used only when constructing the pseudorange-residual input feature, as described in Section 2.2.2.

2.2.2 DGNSS-based multipath labels and feature extraction

The key to supervised learning for multipath prediction is the construction of usable training labels. Since it is not possible to directly obtain the true pseudorange multipath in urban canyons (Zhong et al. 2010), this study uses DGNSS differencing to eliminate clock terms and substantially reduce atmospheric common-mode errors. For epoch t, satellite i, and reference satellite k in the same constellation, given the calibrated receiver ground-truth coordinate p_{true}, the base-station coordinate p_b, and satellite positions computed from broadcast ephemerides, the DD true geometric range can be expressed as

$$\begin{aligned}\Delta\nabla\tilde{\rho}_{rb}^{ik}(t) = &\left(\left\|p_{\text{true}}(t) - p^i(t)\right\| - \left\|p_b - p^i(t)\right\|\right) \\ &-\left(\left\|p_{\text{true}}(t) - p^k(t)\right\| - \left\|p_b - p^k(t)\right\|\right)\end{aligned} \quad (4)$$

where $\Delta\nabla\tilde{\rho}_{rb}^{ik}(t)$ denotes the true double-differenced geometric range between target satellite i and reference satellite k at epoch t; $\boldsymbol{p}_{\text{true}}(t)$ is the ground-truth position of the rover receiver; $\boldsymbol{p}_b$ is the known position of the base station; and $\boldsymbol{p}^i(t)$ and $\boldsymbol{p}^k(t)$ are the positions

of target satellite i and reference satellite k, respectively. All coordinates are expressed in the ECEF frame, and $\|\cdot\|$ denotes the Euclidean norm.

Based on the DD geometric range in (4), the equivalent DD multipath label is constructed as

$$m^{ik}(t) = \Delta\nabla P_{rb}^{ik}(t) - \Delta\nabla \tilde{\rho}_{rb}^{ik}(t) \quad (5)$$

where m^{ik} is the multipath label used in this study. Under short-baseline pseudorange conditions, m^{ik} is mainly composed of DD multipath/NLOS and noise, and may include small residual atmospheric and hardware-delay terms. For the KLT data used here, the baseline length is only several kilometres, so the clock terms are eliminated, while most atmospheric common-mode effects are substantially reduced. The label is therefore still referred to as a multipath label in this study. It shares the same algebraic structure as the unmodeled errors that affect positioning in the differential solver, and can be injected back during positioning to mitigate the corresponding DD multipath effect (Dong et al. 2016).

The extracted multipath's mean absolute values are shown in Fig. 1. Large multipath values are mainly concentrated at elevation angles below 45°. Label construction requires reference-satellite consistency. Since both DD labels and DD positioning depend on the reference satellite *k*, if the reference-satellite selection is inconsistent between training and testing/positioning, model outputs will not match the solver equations and the correction will fail, potentially introducing additional bias. As specified in Section 2.2.1, the highest-elevation satellite in each constellation is consistently used as the reference satellite throughout label construction, model training, and correction injection.

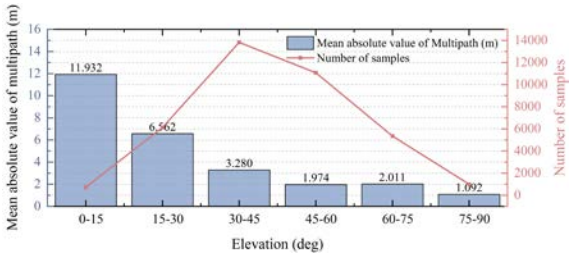


Fig. 1 Statistical analysis of average multipath error based on elevation angle

If the reference satellite is seriously affected by multipath/NLOS, the common term will enter all target-satellite labels. In that case, the present model cannot independently identify which part is introduced only by the reference satellite from the DD labels themselves. A check in the supporting study used G16 and G26 separately as reference satellites for G27, and the two DD multipath series had a correlation coefficient of 0.586. This result indicates that reference-satellite selection changes the label magnitude, while part of the main multipath variation is still retained. Therefore, the highest-elevation reference-satellite strategy reduces but cannot completely remove this risk.

In addition, the formula for calculating coordinate-domain labels is as follows:

$$\Delta \boldsymbol{p}(t) = \boldsymbol{p}_{\text{true}}(t) - \boldsymbol{p}_{\text{W}}(t) \quad (6)$$

where $\boldsymbol{p}_{\text{W}}(t)$ is the weighted DGNSS position estimate. After predicting the position difference, it is added to the baseline DGNSS result:

$$\boldsymbol{p}_{\text{corr}}(t) = \boldsymbol{p}_{\text{W}}(t) + \Delta\hat{\boldsymbol{p}}(t) \quad (7)$$

Feature extraction focuses on observable information that is related to multipath formation. For any satellites, the following feature components are constructed:

(1) Unit observation vector direction, the LOS direction (equivalently satellite direction relative to the receiver);

(2) Elevation, reflecting incidence direction and blockage probability;

(3) C/N0, reflecting signal quality and potential blockage;

(4) DD pseudorange residual, derived from a geometric model. The pseudorange residual feature is derived from an equal-weight DGNSS solution. This choice avoids embedding the elevation- and C/N0-based weighting rule into the residual feature, since elevation and C/N0 are already provided separately as model inputs. Although the residual is not equivalent to the multipath error itself (Zhang et al. 2018), it remains sensitive to multipath/NLOS variations and is therefore included as an input feature.

The model does not explicitly distinguish whether an observation is affected by NLOS or multipath.

In the KLT urban-canyon data, the multipath label mainly reflects the combined influence of multipath and NLOS, while noise and small unmodeled terms remain in the label. C/N0, elevation, LOS direction and DD pseudorange residuals can describe the observation condition, but they are not independent physical labels for signal propagation type.

Building height is not directly used as an input feature in the present experiment because a synchronized three-dimensional building model is not available for the KLT observations. Its influence is only reflected indirectly through elevation, LOS direction, C/N0 and pseudorange residuals. Therefore, the present feature set cannot explicitly describe facade height or street height-to-width ratio.

2.3 GNSS pseudorange multipath modeling

The workflow is organized around two connected calculations. After preprocessing, DD multipath labels are constructed using Equation (5), and the aligned feature sequences are generated for the observation-domain model. An equal-weight DGNSS solution is used only to construct the pseudorange-residual feature. Separately, an elevation-angle- and C/N0-weighted DGNSS solution is obtained as the common positioning baseline. The difference between this weighted baseline solution and the reference trajectory provides the supervision for coordinate-domain correction.

During training, two types of learners are implemented. The coordinate-domain model outputs the position correction $\Delta\hat{\boldsymbol{p}}$, while the observation-domain model outputs the per-satellite DD pseudorange correction (multipath) $\hat{m}(t,s)$. Data organization is closely related to model structure. For CNN-type models, since the number of visible satellites varies over time, satellites must be mapped to a fixed index set at each epoch, and missing satellites are handled by padding values and masks. For GNN-type models, a satellite graph can be constructed per epoch, that is, nodes correspond to visible satellites and node features are the geometric and signal features above, and missing satellites do not require explicit padding.

2.3.1 GCNN

GNNs are suitable for handling satellite sets whose size varies by epoch. For each epoch *t*, a satellite graph $G(t)=(V,E)$ is constructed, where V corresponds to visible satellites and E reflects inter-satellite relations (Bronstein et al. 2017; Scarselli et al. 2009). The node feature vector is defined as

$$x_v=\begin{bmatrix} res, LOS_x, LOS_y, LOS_z, \\ Elevation, C/N_0 \end{bmatrix}^T \tag{8}$$

corresponding to the observation residual, LOS direction, elevation, and carrier-to-noise ratio. The observation-domain output uses node-level regression to produce a DD multipath correction $\hat{m}(t,s)$ (or node-wise corrections). The coordinate-domain output uses graph-level regression to output a position correction $\Delta\hat{\boldsymbol{p}}(t)$ for each epoch.

The GCNN structure is illustrated in Fig. 2. Edges are constructed using a hybrid criterion based on constellation membership, pseudorange-residual similarity, and elevation-angle similarity. Specifically, an edge is established when the two satellites belong to the same constellation, when the absolute difference in their pseudorange residuals is less than 15 m, or when the absolute difference in their elevation angles is less than 10°. This rule allows message passing between satellites that are either from the same constellation or exhibit similar residual or geometric characteristics.

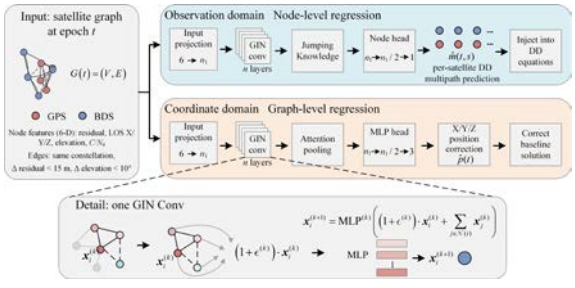


Fig. 2 GCNN architecture

The graph convolution operator follows the message-passing framework, where node

representations are updated layer by layer by aggregating neighborhood information. To increase expressive power, this study uses a Graph Isomorphism Network (GIN) operator with an MLP as the update function (Xu et al. 2018a). For the observation-domain task, Jumping Knowledge is introduced to combine representations from different GIN layers (Xu et al. 2018b). The resulting node representations are fed into a node-level prediction head to obtain a DD multipath correction $\hat{m}(t,s)$ for each satellite. For the coordinate-domain task, the node representations produced by the GIN layers are aggregated through attention pooling to obtain a graph-level representation, which is then mapped by an MLP head to the three-dimensional position correction. It should be emphasized that the observation-domain labels include noise and residual unmodeled terms. Therefore, the observation-domain outputs are interpreted as equivalent DD multipath corrections, and their effectiveness is ultimately judged by whether the positioning error decreases after injection into the DD equations.

2.3.2 CNN

CNNs can model local correlation structures on regular tensors via parameter sharing, and are a direct baseline choice for positioning corrections (Li et al. 2023; Xu et al. 2023). Considering that single-epoch observations can be viewed as a set of satellites, each epoch is organized into a fixed-size satellite–feature matrix. Let the set of satellites appearing in training have size N, and let each satellite have feature dimension *F*. The input at epoch t is $X(t) \in \square^{N \times F}$. Missing satellites are zero-padded, and masks are used to ignore missing or no-ground-truth samples in the loss computation to reduce spurious correlations induced by padding. The output uses either coordinate-domain position corrections or multipath errors as supervision.

The network uses 1D convolutions along the satellite dimension to extract inter-satellite correlation patterns, combined with batch normalization and dropout for training stability and generalization. To keep a clear baseline, the CNN output layer uses linear regression to output corrections.

3 Experiments and results

3.1 Experimental data

The data used in this study are taken from the public urban-scene dataset collected in Kowloon Tong (KLT), Hong Kong (Hu et al 2023). This dataset was collected and released by the team of Li-Ta Hsu at The Hong Kong Polytechnic University. The u-blox F9P receiver recorded GNSS observations at 1 Hz, and the reference trajectory was provided by a post-processed NovAtel SPAN-CPT GNSS/inertial navigation system (INS). The distance from the rover receiver to the HKSC reference station ranges from 3.892 km to 4.319 km. As shown in Fig. 3, the vehicle trajectory in the KLT dataset covers both north-south and east-west road segments, passing through relatively open intersections as well as building-dense and narrow street sections. The KLT1, KLT2 and KLT3 routes are mainly surrounded by low- and medium-rise buildings, trees and dynamic traffic flow, which reflect a relatively light urban canyon environment. In addition, the dataset provides observation data from both the vehicle-mounted receiver and the reference station, together with high-precision ground-truth coordinates corresponding to the vehicle trajectory.

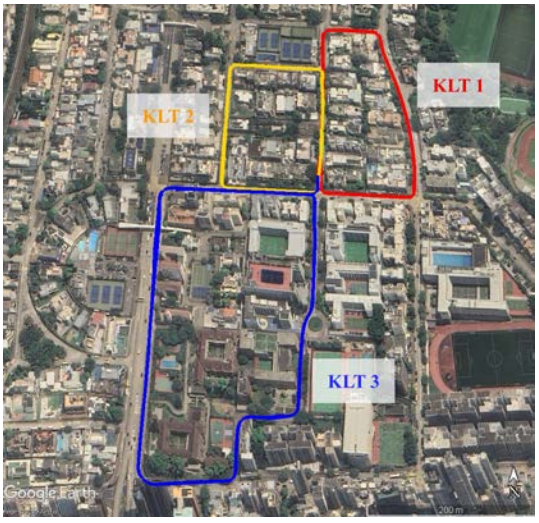


Fig. 3 Ground truth trajectory of the vehicle-mounted receiver

It should be noted that the urban canyon nature of

the KLT dataset does not imply that every epoch is subject to severe signal blockage, since some road segments may still exhibit observation conditions close to open-sky environments.

Table 1 The plane and 3D RMSE of the SPP solution for the ten trajectories (unit: m)

Trajectory	XY plane	3D
0610_KLT1_203	7.403	8.376
0610_KLT2_209	12.933	14.857
0610_KLT3_404	15.542	16.727
1109_KLT1_421	19.712	23.874
1109_KLT2_294	9.686	15.798
1109_KLT2_301	11.161	16.864
1109_KLT3_666	18.955	23.863
1116_KLT1_184	9.806	14.230
1116_KLT2_169	8.800	14.241
1116_KLT3_649	9.614	13.910

Table 1 presents the root mean square error (RMSE) of single point positioning (SPP) results for the ten trajectories included in the dataset. Clearly, the observation environments associated with these trajectories vary in complexity. We selected the "1109_KLT3_666" trajectory as the test set because it contains the highest number of epochs (666) and represents one of the two cases with the greatest environmental complexity and the poorest positioning accuracy, and the data from the remaining nine trajectories were used as the training set. An additional 20% of the epochs from these nine trajectories were randomly selected as a validation set.

3.2 Results

3.2.1 Modeling results of DD pseudorange multipath in the observation domain

There are clear differences between the performance of GCNN and CNN in modeling double-differenced pseudorange multipath in the observation domain. Fig. 4 presents the scatter distributions of GCNN and CNN for observation-domain multipath prediction. Overall, the predictions of both GCNN and CNN follow the variation trend of the ground truth, while GCNN shows a visibly tighter scatter around the diagonal. As shown in Fig. 5, the RMSE values of GCNN and CNN are 3.15 m and 4.85 m, respectively, while their mean absolute error (MAE) values are 2.14 m and 2.65 m, respectively. The coefficient of determination (R^2) also improves from 0.646 for CNN to 0.843 for GCNN, and the bias is reduced in magnitude from -0.42 m to -0.03 m. These results indicate that the graph-structured model more accurately captures the DD multipath variations and provides a better overall fit than the fixed-tensor CNN baseline.

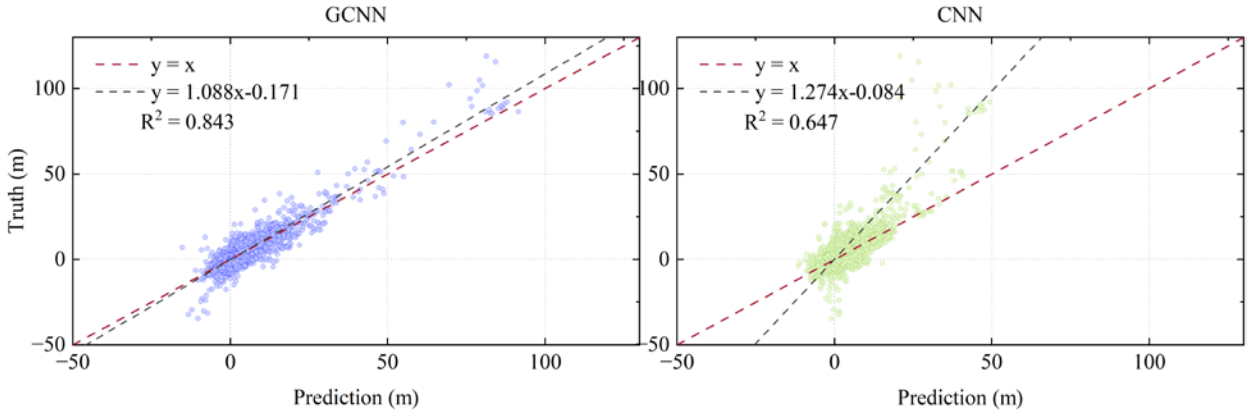


Fig. 4 Scatter plot of multipath error prediction for GCNN and CNN

The improvement of GCNN over CNN is clear in both average and distributional metrics. As shown in Table 2, the overall RMSE decreases from 4.85 m to 3.15 m, corresponding to a reduction of about 35.1%, and the MAE decreases from 2.65 m to 2.14 m. The median absolute error is reduced from 1.71 m to 1.49 m, the 75th percentile of absolute error decreases from 3.24 m to 2.90 m, and the 99th percentile decreases from 15.95 m to 10.41 m. Combined with the violin plots in Fig. 6, these

results indicate that the prediction errors of GCNN are not only smaller on average, but also more concentrated, with a noticeably shorter tail. This suggests that graph-structured aggregation is more effective in capturing multi-satellite error patterns under complex urban environments. The main reason is that GCNN constructs a graph directly from the visible satellites at each epoch, preserves inter-satellite topological relationships during message passing, and exploits correlations among neighboring nodes. This structure is more consistent with the formation mechanism of multipath errors in urban canyons, where errors are influenced by common environmental factors (Zheng et al. 2024). By contrast, although CNN can extract local correlations from a fixed input matrix, its neighborhood relationships are determined by the input arrangement and do not necessarily correspond to the true spatial relationships among satellites.

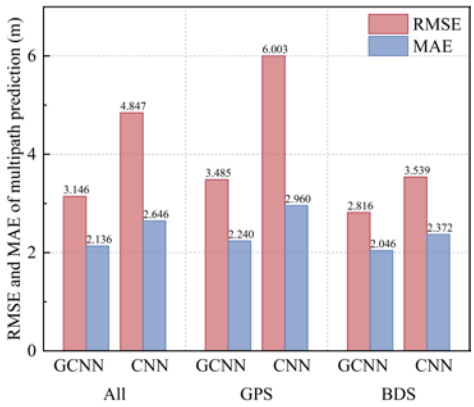


Fig. 5 RMSE and MAE of multipath error prediction for GCNN and CNN by satellite constellation

Fig. 5 and Table 2 present the constellation-wise results. For GPS, the RMSE of GCNN is 3.49 m, clearly lower than the 6.00 m of CNN. For BDS, the RMSE of GCNN is 2.82 m, also lower than the 3.54 m of CNN. Therefore, GCNN outperforms CNN in both constellations, while the magnitude of improvement is more pronounced for GPS. This suggests that the graph-based representation is particularly helpful when the DD multipath error varies more strongly across satellites and epochs.

The larger GPS errors should be understood as a result of the present KLT samples, instead of a general conclusion for GPS. Possible reasons include the sampled satellite elevation distribution, C/N0 distribution, visible-satellite geometry, observation timing and reference-satellite quality. These factors are coupled in the present dataset and cannot be separated quantitatively from the available results. Considering all samples together, GCNN achieves a median absolute error of 1.49 m, lower than the 1.71 m of CNN, and a 75th percentile of 2.90 m, lower than the 3.24 m of CNN. At the 99th percentile, GCNN also remains better, with 10.41 m compared with 15.95 m for CNN. This further shows that the improvement brought by GCNN is reflected not only in the main sample range but also in the control of larger errors.

Table 2 Statistical results of multipath error prediction accuracy for GCNN and CNN by satellite (unit: m)

Model	Constellation	Samples	RMSE	MAE	Bias	STD	Median absolute error	75th percentile of absolute error	99th percentile of absolute error
GCNN	All	8573	3.15	2.14	-0.03	3.15	1.49	2.90	10.41
	GPS	4000	3.49	2.24	0.42	3.46	1.48	3.00	13.02
	BDS	4573	2.82	2.05	-0.42	2.78	1.51	2.81	8.84
CNN	All	8573	4.85	2.65	-0.42	4.83	1.71	3.24	15.95
	GPS	4000	6.00	2.96	-0.36	5.99	1.82	3.35	21.80
	BDS	4573	3.54	2.37	-0.48	3.51	1.62	3.14	12.10

The violin plots in Fig. 6 are consistent with the above statistical results. The error distribution of GCNN is more concentrated and its main body is narrower, whereas the distribution of CNN is slightly wider with a somewhat longer tail. This difference is related to the way the inputs are

organized in the two models. CNN requires satellites to be mapped to fixed index positions, and missing satellites must be padded, so the input structure does not fully match the true relationships among satellites. By contrast, GCNN directly constructs a graph from the visible satellites at each epoch and can preserve inter-satellite relationships during node aggregation. As a result, it is more stable in urban canyon environments where the visible satellite set changes rapidly.

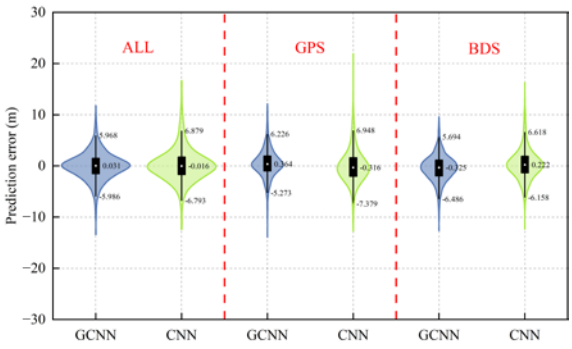


Fig. 6 Violin plot of multipath prediction errors for GCNN and CNN by satellite constellation

Fig. 7 presents the predicted multipath error time series for several selected satellites. From the curve-tracking results, both GCNN and CNN are able to follow the fluctuations of the ground truth at most epochs, while GCNN remains closer to the ground truth around peaks and valleys. This is important because the effect of multipath error on positioning is not reflected only in the mean bias, but also in abrupt changes or continuous deviations over local time intervals. If a model can only provide a smoothed trend but fails to capture the key fluctuations, the positioning benefit after correction will be weakened. Fig. 7 shows that GCNN follows the epoch-wise variations of the DD multipath labels more closely, particularly around several local peaks and valleys.

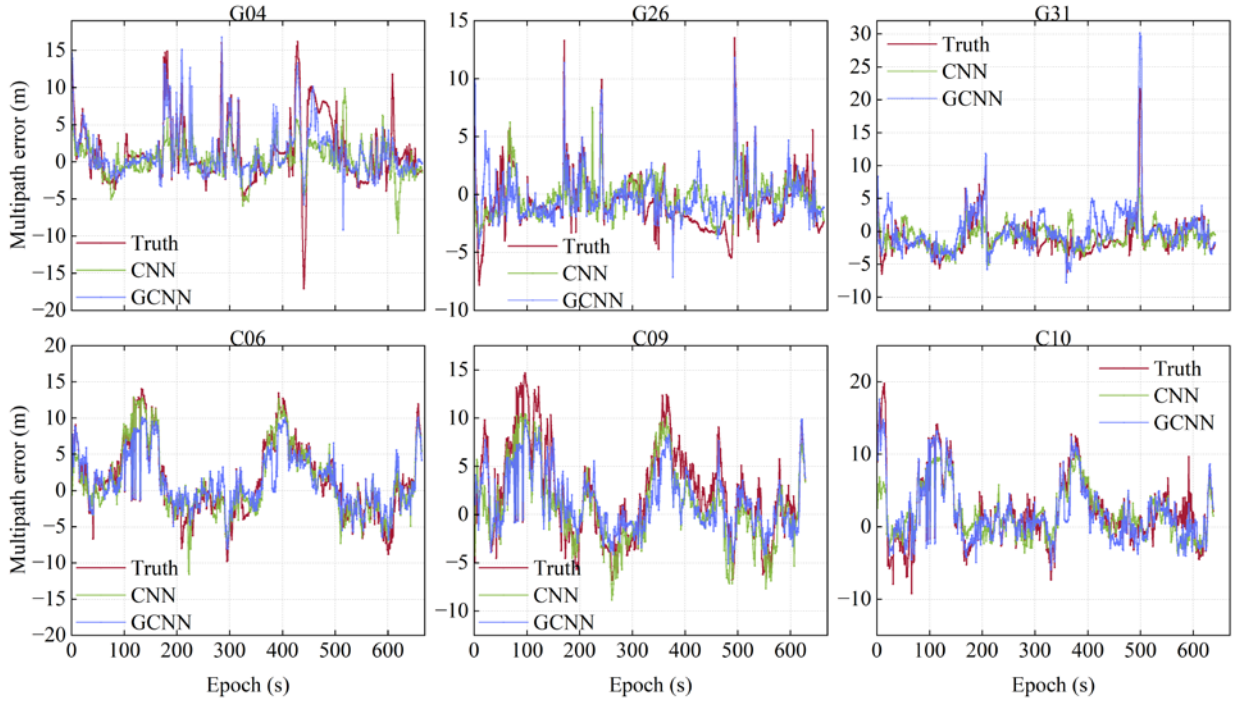


Fig. 7 Epoch-wise DD multipath predictions for selected satellites

Table 3 summarizes the implementation environment and the main training configurations of the two GCNN models. Both models use six-dimensional node features, ReLU activation, AdamW optimization, a batch size of 32, a dropout rate of 0.3, and a weight decay of 1.0×10^{-5}. The observation-domain model contains three graph convolution layers with a hidden dimension of 352 and an initial learning rate of 0.001, whereas the coordinate-domain model uses three graph convolution layers with a hidden dimension of 192 and an initial learning rate of 0.009. Both models employ the Huber loss with δ=10.0 and ReduceLROnPlateau for learning-rate scheduling,

with patience values of 25 and 10 for the observation-domain and coordinate-domain models, respectively.

Table 3 Implementation environment and training configurations of the GCNN models

Parameter	Value	Parameter	Value
Hardware and software			
Programming language	Python 3.9.20	GPU	NVIDIA GeForce RTX 4060 Laptop GPU
Deep learning framework	PyTorch 2.5.1 (CUDA 11.8)	Graph library	PyTorch Geometric 2.6.1
Observation-domain GCNN			
Input feature dimension	6	Graph convolution layers	3
Hidden dimension	352	Dropout	0.3
Activation function	ReLU	Loss function	Huber, δ = 10.0
Output dimension	1	Batch size	32
Optimizer / initial LR	AdamW / 0.001	Weight decay	1.0E-05
LR scheduler	ReduceLROnPlateau (factor 0.5, patience 25, min_lr 1e-6)		
Coordinate-domain GCNN			
Input feature dimension	6	Graph convolution layers	3
Hidden dimension	192	Dropout	0.3
Activation function	ReLU	Loss function	Huber, δ = 10.0
Output dimension	3	Batch size	32
Optimizer / initial LR	AdamW / 0.009	Weight decay	1.0E-05
LR scheduler	ReduceLROnPlateau (factor 0.5, patience 10, min_lr 1e-6)		

3.2.2 Modeling results of positioning correction in the coordinate domain

Fig. 8 and Fig. 9 present the scatter distributions of GCNN and CNN, respectively, for the prediction of positioning corrections in the coordinate domain. Overall, the predictions of both models show good correspondence with the ground truth, indicating that both the graph-structured model and the fixed-tensor model are able to learn statistical patterns related to three-dimensional coordinate errors from the input features. However, judging from the scatter concentration, GCNN exhibits a more compact distribution in the Y and Z directions, with relatively fewer outliers, whereas CNN still shows a certain degree of dispersion in some directions. This suggests that, in the coordinate-domain task, GCNN provides a more balanced fitting of the overall positioning bias. The comparison of RMSE and MAE shown in Fig. 10 is also consistent with the scatter distributions, where GCNN outperforms CNN in the overall three-dimensional metrics.

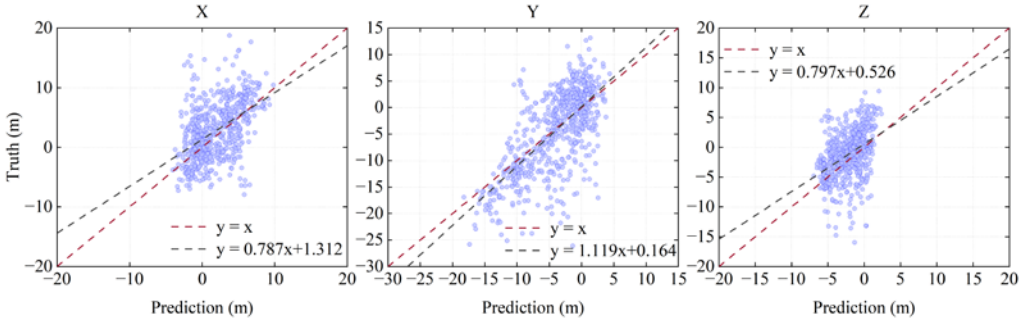


Fig. 8 Scatter plot of GCNN coordinate-domain positioning correction predictions

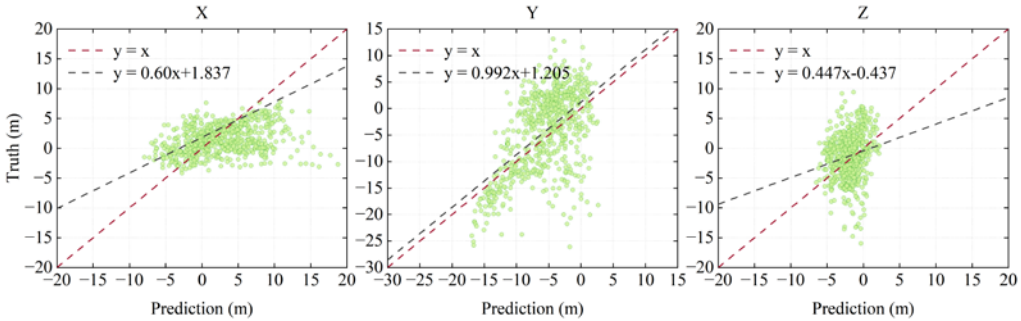


Fig. 9 Scatter plot of CNN coordinate-domain positioning correction predictions

Table 4 provides more detailed statistical results. In terms of the overall three-dimensional metrics, GCNN achieves a 3D RMSE of 7.85 m, lower than the 8.84 m of CNN, while the corresponding MAE values are 6.47 m and 7.54 m, respectively. GCNN also outperforms CNN in all three coordinate components. The RMSE values in the X, Y, and Z directions are 4.23 m, 5.52 m, and 3.62 m for GCNN, compared with 4.73 m, 6.37 m, and 3.90 m for CNN, respectively. These results indicate that graph-structured modeling improves coordinate-domain correction in all three components and provides a more accurate overall position correction

.

Table 4 Prediction accuracy of coordinate-domain positioning correction for GCNN and CNN (unit: m)

Model	Direction	RMSE	MAE	Bias	Std	90th percentile of absolute error	95th percentile of absolute error	99th percentile of absolute error
GCNN	X	4.23	3.17	-0.93	4.13	6.60	8.48	13.44
	Y	5.52	4.20	0.31	5.52	8.39	11.53	16.09
	Z	3.62	2.76	-0.99	3.48	5.66	7.29	10.69
	3D	7.85	6.47	/	4.50	11.43	14.60	23.68
CNN	X	4.73	3.56	-1.23	4.56	7.36	9.05	15.51
	Y	6.37	5.09	-1.25	6.24	10.23	11.85	17.53
	Z	3.90	3.06	-0.61	3.85	6.05	7.32	11.54
	3D	8.84	7.54	/	5.00	12.94	15.23	26.34

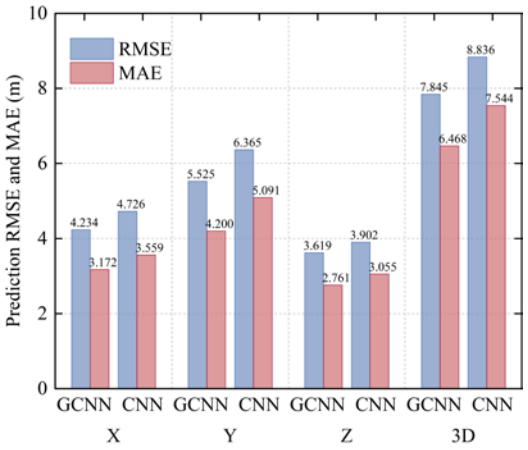


Fig. 10 RMSE and MAE of GCNN and CNN coordinate-domain positioning correction predictions

From the perspective of error quantiles, the 90th, 95th, and 99th percentiles of the three-dimensional absolute error for GCNN are 11.43 m, 14.60 m, and 23.68 m, respectively, all lower than the corresponding CNN values of 12.94 m, 15.23 m, and 26.34 m. This result shows that the advantage of GCNN is reflected not only in lower average errors but also in improved control of larger-error samples.

3.3 Positioning performance of the two correction paths

Fig. 11 presents the epoch-wise variations and error distributions of the X-, Y-, and Z-component positioning errors for the DD baseline and the two GCNN-based correction strategies. Compared with the DD baseline, both correction methods generally shift the error distributions toward zero and reduce their dispersion. In the present test, the coordinate-domain correction produces more concentrated error distributions overall and achieves lower RMSE values in all three coordinate components than the observation-domain correction. In the observation-domain path, the predicted DD pseudorange multipath terms are fed back into the DD observation equations before weighted positioning, whereas the coordinate-domain path directly compensates the weighted baseline position solution. These results indicate that both correction strategies are effective, although the coordinate-domain correction provides the larger overall reduction in positioning error in the present experiment.

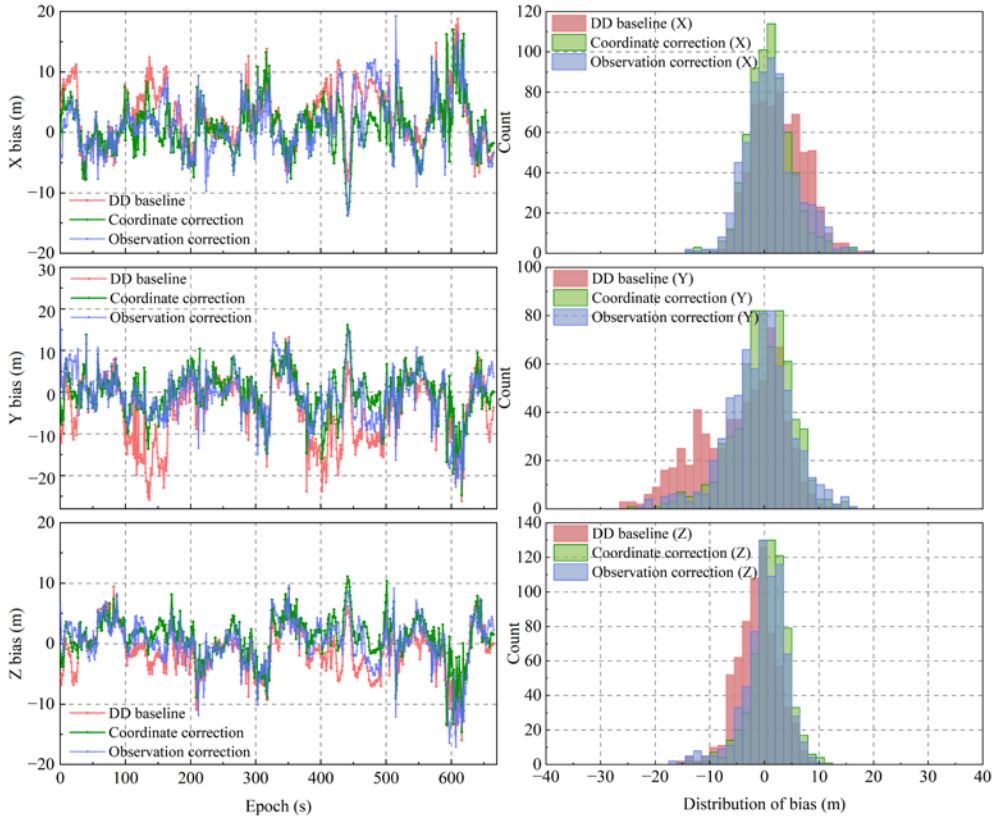


Fig. 11 Time series and distributions of the X-, Y-, and Z-component positioning errors for the DD baseline, GCNN observation-domain correction, and GCNN coordinate-domain correction

According to Tables 4 and 5, the 3D RMSE of the DD baseline is 11.01 m. After GCNN-based observation-domain correction, it decreases to 8.76 m, while coordinate-domain correction further reduces it to 7.85 m. Relative to the common weighted DGNSS baseline, the two correction paths reduce the 3D RMSE by approximately 20.4% and 28.7%, respectively. Therefore, both correction paths improve positioning accuracy, with the coordinate-domain approach yielding the smaller final positioning error in the present test.

The DD baseline RMSE values in the X, Y, and Z directions are 5.42 m, 8.70 m, and 4.03 m, respectively. After observation-domain correction, they decrease to 4.87 m, 6.11 m, and 3.97 m, while coordinate-domain correction further reduces them to 4.23 m, 5.52 m, and 3.62 m. The Y direction exhibits the largest systematic bias in the baseline solution and also shows substantial improvement after correction. Its bias changes from -4.28 m for the baseline to -0.89 m after observation-domain correction and 0.31 m after coordinate-domain correction, while the corresponding standard deviations decrease from 7.57 m to 6.05 m and 5.52 m, respectively. These results show that both correction paths effectively mitigate the dominant Y-direction error, with the coordinate-domain correction yielding the smallest RMSE and standard deviation in the present test.

Table 5 Statistical results of the DD baseline and observation-domain corrected positioning (unit: m)

Method	Direction	RMSE	Bias	Std	90th percentile of absolute error	95th percentile of absolute error	99th percentile of absolute error
DD Baseline	X	5.42	2.73	4.68	8.82	10.17	14.75
	Y	8.70	-4.28	7.57	15.45	17.90	22.44
	Z	4.03	-1.28	3.82	6.30	7.53	12.83
	3D	11.01	/	6.27	17.90	20.50	26.56
Observation-domain correction	X	4.87	1.22	4.71	8.33	10.20	13.83
	Y	6.11	-0.89	6.05	9.75	12.59	18.19
	Z	3.97	0.15	3.96	6.06	8.26	13.07
	3D	8.76	/	5.07	13.28	16.35	27.02

Quantile analysis further shows that the positioning-error distribution is improved after correction. For the 3D positioning error, the 90th and 95th percentiles of the DD baseline are 17.90 m and 20.50 m, respectively. They decrease to 13.28 m and 16.35 m after observation-domain correction and to 11.43 m and 14.60 m after coordinate-domain correction. At the 99th percentile, the observation-domain result is 27.02 m, slightly higher than the baseline value of 26.56 m, whereas the coordinate-domain correction reduces it to 23.68 m. Thus, the coordinate-domain approach provides a more consistent improvement across both the main body and the upper tail of the error distribution, while a small number of extreme observation-domain correction errors remain.

Fig. 12 further compares the cumulative distribution functions (CDFs) of the 3D positioning errors obtained from the DD baseline and the two GCNN-based correction methods. Over most of the probability range, both corrected solutions shift toward smaller positioning errors relative to the DD baseline. Among the three solutions, the coordinate-domain correction generally exhibits the leftmost and uppermost CDF curve, indicating the highest probability of satisfying a given positioning-accuracy threshold. The observation-domain correction also provides a clear improvement over the DD baseline over most of the distribution, although its overall error

distribution is slightly less favorable than that of the coordinate-domain correction.

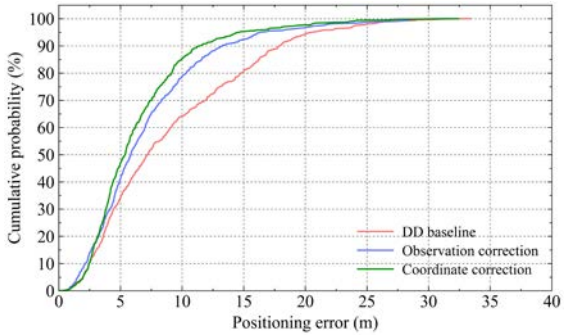


Fig. 12 CDFs of 3D positioning errors before and after GCNN-based correction

This tendency is consistent with the statistical results in Tables 4 and 5. The coordinate-domain correction achieves the smallest 90th-, 95th-, and 99th-percentile 3D positioning errors, with values of 11.43 m, 14.60 m, and 23.68 m, respectively. The observation-domain correction also reduces the 90th and 95th percentiles to 13.28 m and 16.35 m, although its 99th-percentile error remains slightly higher than that of the DD baseline. These results indicate that the coordinate-domain correction provides the most consistent improvement over the overall positioning-error distribution in the present experiment.

4. Discussion

The observation-domain and coordinate-domain correction paths differ in both their learning targets and the stage at which the learned corrections are introduced. The observation-domain model performs node-level regression to predict a satellite-wise DD pseudorange multipath term, whereas the coordinate-domain model performs graph-level regression to estimate a three-dimensional position correction from the aggregated satellite representation. Accordingly, the observation-domain target is more closely related to the error term in the DD observation equation, while the coordinate-domain target represents the resulting positioning error and therefore also contains the effects of satellite geometry, observation noise, weighting strategy, and the positioning solver. The two targets are related through the positioning model but should not be regarded as equivalent numerical quantities. This distinction leads to different advantages and limitations. The observation-domain approach operates closer to the measurement level. If the DD pseudorange errors can be predicted accurately, the corrections can be incorporated into different positioning estimators while preserving the physical structure of the observation equations (Zhong et al. 2010; Pan et al. 2024). However, any residual prediction error remaining in the corrected observations is still propagated into the coordinate solution through the satellite geometry. Therefore, the same level of residual observation error may produce different positioning effects under different geometric configurations. In contrast, the coordinate-domain approach directly predicts the position correction and thus bypasses this explicit propagation of observation-domain prediction residuals through the geometric design matrix (Xu et al. 2023). This shorter end-to-end path reduces the direct exposure of the correction process to geometric amplification and jointly captures the effects of observation errors, satellite geometry, weighting, and the positioning solver. However, this joint mapping is less directly interpretable at the observation level and may be more dependent on the conditions represented in the training data.

The experimental results are consistent with these differences between the two correction paths. In the present test, the coordinate-domain correction achieves the smallest final positioning error, reducing the 3D RMSE from 11.01 m for the weighted DD baseline to 7.85 m, compared with 8.76 m after observation-domain correction. The coordinate-domain approach also yields smaller 90th-, 95th-, and 99th-percentile errors than the observation-domain approach. This result suggests that directly learning the position correction provides a more effective end-to-end mapping under the current data and positioning configuration. However, it should not be interpreted as evidence that the coordinate-domain approach is inherently superior. The observation-domain approach retains stronger physical interpretability and allows the predicted corrections to be introduced directly into the

observation equations and subsequently processed by the positioning estimator.

The two correction paths are evaluated separately in this paper. Directly adding the observation-domain and coordinate-domain corrections may count part of the same error twice, because the coordinate-domain label already contains the position effect of the observation-domain multipath error. A reasonable combination needs a new sequential or gated fusion model, for example learning the remaining position error after observation-domain correction. Such a model is not included in the present experiment and will be considered in later work.

Although Table 3 reports the final model configurations of GCNN, the present study does not include a complete component ablation. A full ablation should independently examine the contributions of feature groups, graph construction, and pooling strategies under identical data splits and repeated training settings.

5. Conclusion

This study adopts a GCNN-based method for GNSS multipath mitigation in urban canyons. Multipath labels are constructed using a GPS/BDS short-baseline pseudorange double-differenced model. Two correction paths are validated, namely the observation domain and the coordinate domain. The main findings are summarized below.

(1) The GCNN outperforms the CNN in both tasks. In the observation domain, the GCNN achieves a multipath prediction RMSE of 3.15 m, compared with 4.85 m for the CNN. In the coordinate domain, the 3D correction RMSE of GCNN is 7.85 m, lower than the 8.84 m obtained by CNN. These results demonstrate that graph-structured representation is effective for both observation-domain multipath modeling and coordinate-domain position correction.

(2) Both correction paths improve positioning accuracy relative to the common weighted DGNSS baseline, while the coordinate-domain path provides the better final result in the present test. The baseline 3D RMSE of 11.01 m is reduced to 8.76 m after observation-domain correction and to 7.85 m after coordinate-domain correction. The coordinate-domain approach also reduces the 90th-, 95th-, and 99th-percentile errors to 11.43 m, 14.60 m, and 23.68 m, respectively, indicating improvement in both the main body and the upper tail of the positioning-error distribution.

(3) The two correction paths have complementary advantages. The observation-domain approach provides stronger physical interpretability and can be readily integrated with conventional GNSS estimators. The coordinate-domain approach directly learns the position correction from joint multi-satellite information and can capture the combined effects of inter-satellite error patterns and positioning geometry. Therefore, neither approach is inherently superior, and their relative performance depends on the specific positioning conditions.

In summary, this study validates the effectiveness of GCNN-based GNSS multipath mitigation in urban canyons through dual-domain correction. The present test is based on one urban dataset, and future work will further consider multi-city data, direct NLOS annotations, map-derived building features, robust reference-satellite screening, fusion of the two correction paths, and controlled component ablation.

Acknowledgements

This work was supported by the Key Program of the Natural Science Foundation of Jiangsu Province, China (Grant No. BK20253016). The authors gratefully acknowledge the research team at The Hong Kong Polytechnic University for publicly providing the NLOS dataset, and the Geodetic Survey Section of the Survey and Mapping Office (SMO), Hong Kong, for providing access to the reference station data.

References

Bronstein M M, Bruna J, LeCun Y, Szlam A, and Vandergheynst P (2017), ***Geometric deep learning: Going beyond euclidean data***. IEEE Signal Processing Magazine 34(4):18-42.

Dong D, Wang M, Chen W, Zeng Z, Song L, Zhang Q, Cai M, Cheng Y, and Lv J (2016), ***Mitigation of multipath effect in GNSS short baseline***

positioning by the multipath hemispherical map. Journal of Geodesy 90(3):255-262.

Groves P D, and Jiang Z (2013), ***Height aiding, C/N0 weighting and consistency checking for GNSS NLOS and multipath mitigation in urban areas***. Journal of Navigation 66(5):653-669.

Guillard A, Thevenon P, and Milner C (2023), ***Using Convolutional Neural Networks to detect GNSS multipath***. Frontiers in Robotics and AI 10, 1106439.

Hu R, Wen W, and Hsu L-T (2023), ***Fisheye camera aided GNSS NLOS detection and learning-based pseudorange bias correction for intelligent vehicles in urban canyons***. In 2023 IEEE 26th international conference on intelligent transportation systems (ITSC) (pp. 6088-6095). IEEE.

Hsu L-T (2017), ***Analysis and modeling GPS NLOS effect in highly urbanized area***. GPS Solutions 22(1):7.

Jiang Z, Groves P D, Ochieng W Y, Feng S, Milner C D, and Mattos P G (2011), ***Multi-constellation GNSS multipath mitigation using consistency checking***, paper presented at Proceedings of the 24th international technical meeting of the satellite division of the institute of navigation (ION GNSS 2011).

Li F, Zhai C, Xie T, Dai Z, and Zhu X (2024), ***GNSS positioning enhancement based on NLOS signal detection using spatio-temporal learning in urban canyons***. GPS Solutions 28(4):209.

Li H, Borhani-Darian P, Wu P, and Closas P (2023), ***Deep Neural Network correlators for GNSS multipath mitigation***. IEEE Transactions on Aerospace and Electronic Systems 59(2):1249-1259.

Lu R, Chen W, Dong D, Wang Z, Zhang C, Peng Y, and Yu C (2021), ***Multipath mitigation in GNSS precise point positioning based on trend-surface analysis and multipath hemispherical map***. GPS Solutions 25(3):119.

Lu R, Chen W, Li Z, Dong D, Jiang W, Wang Z, Huang L, and Duan X (2023), ***An improved joint modeling method for multipath mitigation of GPS, BDS-3, and Galileo overlapping frequency signals in typical environments***. Journal of Geodesy 97(10):95.

Mohanty A, and Gao G (2023), ***Learning GNSS positioning corrections for smartphones using Graph Convolution Neural Networks***. NAVIGATION 70(4):navi.622.

Mohanty A, and Gao G (2024), ***A survey of machine learning techniques for improving Global Navigation Satellite Systems***. EURASIP Journal on Advances in Signal Processing 2024(1):73.

Pan Y, Möller G, and Soja, B (2024), ***Machine learning-based multipath modeling in spatial domain applied to GNSS short baseline processing***. GPS Solutions 28(1):9.

Scarselli F, Gori M, Tsoi A C, Hagenbuchner M, and Monfardini G (2009), ***The Graph Neural Network Model***. IEEE Transactions on Neural Networks 20(1):61-80.

Tay S, and Marais J (2013), ***Weighting models for GPS Pseudorange observations for land transportation in urban canyons***. In 6th European workshop on GNSS signals and signal processing (p. 4p).

Teunissen P J, and Montenbruck O (2017), ***Springer handbook of global navigation satellite systems***, Springer

Wang M, Wang J, Dong D, Chen W, Li H, and Wang Z (2018), ***Advanced sidereal filtering for mitigating multipath effects in GNSS short baseline positioning***, ISPRS International Journal of Geo-Information, 7(6), 228

Xu K, Hu W, Leskovec J, and Jegelka S (2018a), ***How powerful are graph neural networks?***. arXiv preprint arXiv:1810.00826.

Xu K, Li C, Tian Y, Sonobe T, Kawarabayashi K I, and Jegelka S (2018b), ***Representation learning on graphs with jumping knowledge networks***. In International conference on machine learning (pp. 5453-5462). pmlr.

Xu P, Zhang G, Yang B, and Hsu L-T (2023), ***PositionNet: CNN-based GNSS positioning in urban areas with residual maps***. Applied Soft Computing 148:110882.

Ye F, Pan S, Gao W, Wang H, Liu G, Ma C, and

Wang Y (2020), ***An improved single-epoch GNSS/INS positioning method for urban canyon environment based on real-Time DISB estimation***. IEEE Access 8:227566-227578.

Zhang Z, Li B, Shen Y, Gao Y, and Wang M (2018), ***Site-specific unmodeled error mitigation for GNSS positioning in urban environments using a real-time adaptive weighting model***. Remote Sensing 10(7): 1157

Zheng S, Zeng K, Li Z, Wang Q, Xie K, Liu, Ming, and Xie S (2024), ***Improving the prediction of GNSS satellite visibility in urban canyons based on a graph transformer***. NAVIGATION: Journal of the Institute of Navigation 71(4).

Zhong P, Ding X, Yuan L, Xu Y, Kwok K, and Chen Y (2010), ***Sidereal filtering based on single differences for mitigating GPS multipath effects on short baselines***. Journal of Geodesy 84(2):145-158.

Authors



Chenkang Cui received the B.S. degree in surveying and mapping engineering from Nanjing Tech University, Nanjing, China, in 2023. He is currently pursuing the M.S. degree in civil and hydraulic engineering at Nanjing Tech University, Nanjing, China. His research interests include deep learning for multipath mitigation.



Yan Xia received the Ph.D. degree in instrument science and technology from Southeast University, Nanjing, China, in 2021. He is currently a lecturer with the School of Geomatics Science and Technology, Nanjing Tech University. His research interests mainly include context awareness, GNSS high-precision positioning in complex environments and indoor positioning.



Bin Wang received the M.S. degree in geodesy and surveying engineering from the China University of Mining and Technology, Xuzhou, China, in 2013, and the Ph.D. degree in geodesy and surveying engineering with the School of Geodesy and Geomatics, Wuwan University, Wuhan, China, in 2017. He is currently a professor with the School of Geomatics Science and Technology, Nanjing Tech University. From 2015 to 2016, he was an exchange visitor supported by DAAD Thematic Network Project with the Institute of Geodesy, University of Stuttgart, Germany. His research interests include generalized total least-squares algorithms and point cloud data processing.